Intrinsic and extrinsic anomalous transport properties in noncollinear antiferromagnetic Mn₃Sn from first-principles calculations

Xiuxian Yang [1,2] Wanxiang Feng,[1,*] Xiaodong Zhou,[2] Yuriy Mokrousov,[3,4] and Yugui Yao [1,†]

[1]*Key Lab of Advanced Optoelectronic Quantum Architecture and Measurement (MOE), Beijing Key Lab of Nanophotonics & Ultrafine Optoelectronic Systems, and School of Physics, Beijing Institute of Technology, Beijing 100081, China*

[2]*Laboratory of Quantum Functional Materials Design and Application, School of Physics and Electronic Engineering, Jiangsu Normal University, Xuzhou 221116, China*

[3]*Institute of Physics, Johannes Gutenberg University Mainz, 55099 Mainz, Germany*

[4]*Peter Grünberg Institut and Institute for Advanced Simulation, Forschungszentrum Jülich and JARA, 52425 Jülich, Germany*

Mn₃Sn has garnered significant attention due to its kagome lattice, 120° noncollinear antiferromagnetic order, and substantial anomalous Hall effect. In this study, we comprehensively explore intrinsic and extrinsic contributions to anomalous Hall, anomalous Nernst, and anomalous thermal Hall effects, employing first-principles calculations and group theory analysis. Comparative analysis between our theoretical results and available experimental data underscores the predominance of the intrinsic mechanism in shaping anomalous transport properties at low temperatures. Specifically, Weyl fermions are identified as the primary contributors to intrinsic anomalous Hall conductivity. The significance of extrinsic mechanisms becomes evident at high temperatures, especially when the longitudinal charge conductivity falls into the dirty regime, where the side jump mechanism plays a vital role. Extrinsic contributions to anomalous transport properties are primarily influenced by the electronic states residing at the Fermi surfaces. Furthermore, anomalous transport properties exhibit periodic variations when subjected to spin rotations within the kagome plane, achievable by applying an external magnetic field. Our findings advance the understanding of anomalous transport phenomena in Mn₃Sn and offer insights into potential applications of noncollinear antiferromagnetic materials in spintronics and spin caloritronics.

I. INTRODUCTION

The anomalous Hall effect (AHE), discovered by Hall in 1881, refers to the emergence of a transverse charge current in response to a longitudinal electric field without the presence of an external magnetic field [1]. It remains a fundamental aspect of condensed matter physics, shedding light on the intricate nature of magnetism [2]. Over time, the understanding of the physical mechanisms underlying AHE has evolved, dividing the effect into intrinsic and extrinsic components. The intrinsic mechanism, which is not influenced by electron scattering, was initially proposed by Karplus and Luttinger [3] and is now well explained by Berry phase theory, relying solely on the electronic band structure of pristine crystals [4,5]. In contrast, the extrinsic mechanisms, such as skew scattering [6,7] and side jump [8], hinge on electron scattering caused by impurities or disorder. Moreover, there are two other remarkable anomalous transport phenomena: the anomalous Nernst effect (ANE) [9] and the anomalous thermal Hall effect (ATHE) [10], which involve the emergence of transverse charge and heat currents driven by longitudinal temperature gradients, respectively. Analogous to the anomalous Hall conductivity (AHC) σ_{ij}, the anomalous Nernst conductivity (ANC) α_{ij}

and anomalous thermal Hall conductivity (ATHC) κ_{ij} can be decomposed into three distinct parts:

$$\sigma_{ij} = \sigma_{ij}^{\text{int}} + \sigma_{ij}^{\text{sj}} + \sigma_{ij}^{\text{isk}}, \tag{1}$$

$$\alpha_{ij} = \alpha_{ij}^{\text{int}} + \alpha_{ij}^{\text{sj}} + \alpha_{ij}^{\text{isk}}, \tag{2}$$

$$\kappa_{ij} = \kappa_{ij}^{\text{int}} + \kappa_{ij}^{\text{sj}} + \kappa_{ij}^{\text{isk}}. \tag{3}$$

Here, the subscripts $i, j \in x, y, z$ represent Cartesian coordinates, and the superscripts int, sj, and isk denote the intrinsic, side jump, and skew scattering contributions, respectively.

The AHE is commonly observed in ferromagnetic conductors, and it is assumed to be proportional to the magnetization. In contrast, antiferromagnets (AFMs) have long been considered to lack the AHE due to their zero net magnetization [11–18]. However, recent advancements have challenged this notion. For example, a significant AHC was predicted in the noncollinear antiferromagnet Mn₃Ir through a combination of symmetry analysis and first-principles calculations [19]. Subsequent experiments confirmed substantial AHC in noncollinear AFMs Mn₃X (X = Sn, Ge) even in the absence of an external magnetic field [20–22]. Compared to ferromagnets, AFMs exhibit an array of exotic properties, including insensitivity to magnetic-field perturbations [23,24], ultrafast spin dynamics [25], and high-frequency uniform spin precession [26–28]. These attributes position AFMs as an excellent platform for antiferromagnetic spintronics [29,30].

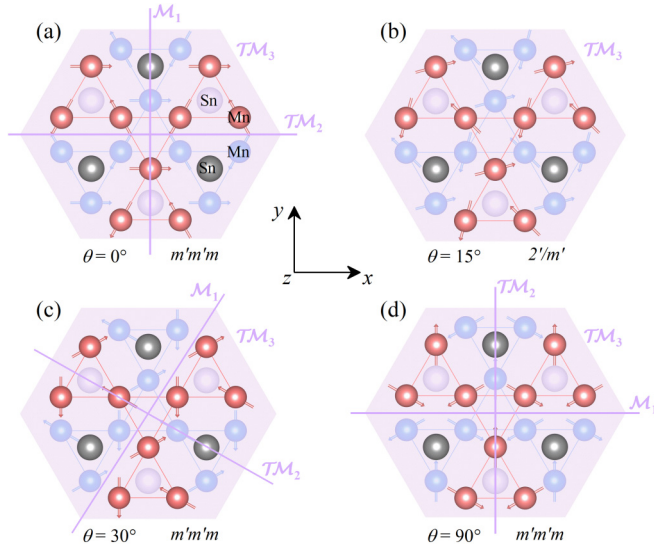*wxfeng@bit.edu.cn

†ygyao@bit.edu.cn

FIG. 1. The crystal and magnetic structure of noncollinear antiferromagnetic Mn_3Sn. The Mn atoms on the upper and lower kagome planes are marked in red and blue, respectively. Within the kagome plane, all spins can be uniformly rotated by an angle θ. The magnetic point groups at different θ are (a) $m'm'm$ at $\theta = 0°$, (b) $2'/m'$ at $\theta = 15°$, (c) $m'm'm$ at $\theta = 30°$, and (d) $m'm'm$ at $\theta = 90°$. These spin configurations are characterized by specific symmetry elements: $\mathcal{M}_1$, denoting a mirror plane perpendicular to the kagome plane; $\mathcal{TM}_2$, representing a combined symmetry with the time-reversal symmetry $\mathcal{T}$ and a mirror plane $\mathcal{M}_2$ perpendicular to the kagome plane; and $\mathcal{TM}_3$, representing a combined symmetry with $\mathcal{T}$ and a mirror plane $\mathcal{M}_3$ parallel to the kagome plane.

Mn_3X, as a representative family of noncollinear AFMs, has garnered significant attention due to its intriguing features, including substantial AHE [20–22,31,32], ANE [33,34], magneto-optical effects [35,36], magnetic Weyl fermions [37,38], the magnetic spin Hall effect [39], and spin-orbit torque [40,41]. Moreover, Mn_3X possesses a unique breathing-type kagome lattice structure formed by Mn atoms, as shown in Fig. 1. This lattice hosts intriguing topological electronic bands, superconducting phases, and strong electromagnetic and transport responses [42–44], making it an ideal platform for exploring novel states of quantum matter. However, previous theoretical investigations on Mn_3X [19,45–48] have primarily focused on the anomalous transport properties induced by the intrinsic Berry curvature mechanism, with limited attention paid to the extrinsic mechanisms related to the scattering of electrons off impurities or disorder. In reality, understanding the contribution of extrinsic mechanisms to the AHE in kagome materials is crucial. For instance, remarkable AHE values ranging from 10^4 to 10^5 S/cm, driven by extrinsic mechanisms, have been discovered in other kagome materials such as KV_3Sb_5 [49], CsV_3Sb_5 [50], and Nd_3Al [51]. These observations underscore the predominant role played by extrinsic mechanisms in governing the AHE, ANE, and ATHE in kagome antiferromagnetic materials.

In this work, we conduct a comprehensive investigation of the intrinsic and extrinsic mechanisms of anomalous transport properties, including the AHE, ANE, and ATHE, in the noncollinear antiferromagnet Mn_3Sn, using state-of-the-art first-principles calculations. By collectively rotating all spins within the kagome plane, we discern the tensor shapes of AHC, ANC, and ATHC through magnetic group theory. For nonzero tensor elements, we compute the intrinsic, side jump, and skew scattering contributions individually. Profound anisotropy in the AHE, intricately connected to the evolving coplanar noncollinear spin configurations, is unveiled. Through careful comparisons with available experimental data, we establish the consistent prevalence of the intrinsic mechanism in driving the AHE at low temperatures, notably when the longitudinal conductivity exceeds 10^4 S/cm. Our study highlights the influential role of Weyl fermions near the Fermi energy in shaping the intrinsic AHC in Mn_3Sn. Nevertheless, we also observe a significant increase in the impact of extrinsic mechanisms, especially the side jump component, as the longitudinal conductivity falls below 10^4 S/cm. The extrinsic AHC predominantly emanates from electronic states positioned precisely at the Fermi surface sheets. Furthermore, our calculations of ANC and ATHC, as well as the anomalous Lorentz ratio, consistently align with experimental observations at low temperatures. Through these findings, we advance the understanding of the intricate competition between intrinsic and extrinsic mechanisms that govern anomalous transport phenomena in the realm of noncollinear antiferromagnetic Mn_3Sn.

II. THEORY AND COMPUTATIONAL DETAILS

The AHE, ANE, and ATHE are interconnected through the generalized Landauer-Büttiker formalism [52–54] as expressed by the anomalous transport coefficients:

$$R_{ij}^{(n)} = \int_{-\infty}^{\infty} (E - \mu)^n \left(-\frac{\partial f}{\partial E} \right) \sigma_{ij}(E) dE, \tag{4}$$

where μ is the chemical potential, $f = 1/\{\exp[(E - \mu)/k_B T] + 1\}$ represents the Fermi-Dirac distribution function, and σ_{ij} is the AHC at zero temperature. The temperature-dependent AHC, ANC, and ATHC can be expressed as follows:

$$\sigma_{ij}^T = R_{xy}^{(0)}, \tag{5}$$

$$\alpha_{ij}^T = -R_{ij}^{(1)}/eT, \tag{6}$$

$$\kappa_{ij}^T = R_{ij}^{(2)}/e^2 T. \tag{7}$$

From Eqs. (4) to (7), it is evident that the zero-temperature AHC σ_{ij} plays a crucial role in determining the other anomalous transport properties.

Following the Kubo formalism within the linear-response theory [55], the AHC can be partitioned into Fermi surface (σ_{ij}^I) and Fermi sea (σ_{ij}^{II}) components [56]:

$$\sigma_{ij}^I = -\frac{e^2 \hbar}{2\pi} \int \frac{d^3 k}{2\pi^3} \sum_{m \neq n} \text{Im}[v_{mn}^i(\mathbf{k}) v_{nm}^j(\mathbf{k})]$$

$$= \frac{(E_{m\mathbf{k}} - E_{n\mathbf{k}})\Gamma}{[(E_f - E_{m\mathbf{k}})^2 + \Gamma^2][(E_f - E_{n\mathbf{k}})^2 + \Gamma^2]} \tag{8}$$

and

$$\sigma_{ij}^{\mathrm{II}} = \frac{e^2 \hbar}{\pi} \int \frac{\mathrm{d}^3 k}{(2\pi)^3} \sum_{m \neq n} \mathrm{Im}\big[v_{mn}^i(\mathbf{k}) v_{nm}^j(\mathbf{k}) \big]$$

$$= \left\{ \frac{\Gamma}{(E_{m\mathbf{k}} - E_{n\mathbf{k}})[(E_f - E_{m\mathbf{k}})^2 + \Gamma^2]} \right.$$
$$\left. - \frac{1}{(E_{m\mathbf{k}} - E_{n\mathbf{k}})^2} \mathrm{Im}\left[\ln \frac{E_f - E_{m\mathbf{k}} + \mathbf{i}\Gamma}{E_f - E_{n\mathbf{k}} + \mathbf{i}\Gamma} \right] \right\}, \quad (9)$$

where $i, j \in x, y, z$ represent Cartesian coordinates, v is the velocity operator, E_f is the Fermi energy, $E_{n\mathbf{k}}$ is the energy eigenvalue with band index n at momentum $\mathbf{k}$, and Γ is an adjustable smearing parameter (0–0.09 eV). This constitutes the constant smearing (CS) model, which describes the intrinsic AHE. In this model, a constant Γ parameter is assigned, providing all electronic states with the same finite lifetime. In the clean limit (i.e., $\Gamma \to 0$), the summation of Eqs. (8) and (9) converges to the well-established Berry curvature expression [5]:

$$\sigma_{ij}^{\mathrm{int}} = e^2 \hbar \int \frac{\mathrm{d}^3 k}{(2\pi)^3} \sum_{n,m \neq n}^{\mathrm{occ}} \frac{2\mathrm{Im}\big[v_{mn}^i(\mathbf{k}) v_{nm}^j(\mathbf{k}) \big]}{(E_{m\mathbf{k}} - E_{n\mathbf{k}})^2}. \quad (10)$$

It should be noted that the complex scattering mechanisms are not explicitly considered within the CS model.

Alternatively, the inclusion of a short-range Gaussian disorder potential allows for the consideration of scattering-dependent AHC, encompassing the side jump and skew scattering mechanisms. Within the Gaussian disorder (GD) model, the impurity potential is described as

$$V = U \sum_i^N \delta(\mathbf{r} - \mathbf{R}_i), \quad (11)$$

where U signifies the scattering strength, δ is the delta function, and $\mathbf{R}_i$ corresponds to the ith random atomic position among a total of N impurities. Consequently, the impurity concentration is denoted as $n_i = N/V$, with V being the volume of the cell. For convenience, the disorder parameter is expressed as $\mathcal{V} = U^2 n_i$ (0–80 eV$^2 a_0^3$). It is crucial to emphasize that this impurity potential is spin independent as it does not encompass spin degrees of freedom. With the incorporation of spin-orbit coupling, the electron's spin becomes intricately reliant on the modification of its orbital angular momentum during scattering. Although the impurity potential utilized in this context can be interpreted only as nonmagnetic impurities in magnetic materials, the possibility of a transverse flow of spin-polarized electrons induced by scattering (i.e., extrinsic anomalous Hall conductivity) is feasible, as demonstrated in previous works [57,58].

The self-energy $\Sigma(E, \mathbf{k})$, which accounts for the impact of electron scattering off impurities, can be expressed as follows, truncated to the lowest order [56]:

$$\Sigma(E, \mathbf{k}) = \mathcal{V} \int \frac{\mathrm{d}^3 k'}{(2\pi)^3} O_{\mathbf{k}\mathbf{k}'} G_0(E, \mathbf{k}') O_{\mathbf{k}'\mathbf{k}}. \quad (12)$$

Here, $O_{\mathbf{k}\mathbf{k}'}$ represents the overlap matrix for the eigenstates at different momenta, and $G_0(E, \mathbf{k}') = [E - H(\mathbf{k}')]^{-1}$ stands for the bare Green's function with the unperturbed Hamiltonian $H(\mathbf{k}')$.

After accounting for the scattering effects, the AHC can be formulated using the full Green's functions $G^{R/A}$ (R: retarded and A: advanced) [56] as follows:

$$\sigma_{ij}^{\mathrm{I}} = \frac{e^2 \hbar}{4\pi} \int \frac{\mathrm{d}^3 k}{(2\pi)^3} \mathrm{Tr}[\Gamma^i(E_f, \mathbf{k}) G^R(E_f, \mathbf{k}) v^j G^A(E_f, \mathbf{k})$$
$$- (i \leftrightarrow j)] \quad (13)$$

and

$$\sigma_{ij}^{\mathrm{II}} = \frac{e^2 \hbar}{2\pi} \int \frac{\mathrm{d}^3 k}{(2\pi)^3} \int_{-\infty}^{E_f} \mathrm{Re}\{\mathrm{Tr}[\Gamma^i(E, \mathbf{k}) G^R(E, \mathbf{k})$$
$$\times \gamma(E, \mathbf{k}) G^R(E, \mathbf{k}) \Gamma^j(E, \mathbf{k}) G^R(E, \mathbf{k})$$
$$- (i \leftrightarrow j)]\}\mathrm{d}E. \quad (14)$$

Here, $\gamma(E, \mathbf{k})$ and $\mathbf{\Gamma}(E, \mathbf{k})$ are scalar and vector vertex functions, respectively, defined as

$$\gamma(E, \mathbf{k}) = I + \mathcal{V} \int \frac{\mathrm{d}^3 k'}{(2\pi)^3} O_{\mathbf{k}\mathbf{k}'} G^R(E, \mathbf{k}') \gamma(E, \mathbf{k}')$$
$$\times G^R(E, \mathbf{k}') O_{\mathbf{k}'\mathbf{k}} \quad (15)$$

and

$$\mathbf{\Gamma}(E, \mathbf{k}) = \mathbf{v}(\mathbf{k}) + \mathcal{V} \int \frac{\mathrm{d}^3 k'}{(2\pi)^3} O_{\mathbf{k}\mathbf{k}'} G^A(E, \mathbf{k}') \mathbf{\Gamma}(E, \mathbf{k}')$$
$$\times G^R(E, \mathbf{k}') O_{\mathbf{k}'\mathbf{k}}, \quad (16)$$

where I and $\mathbf{v}$ are identity and velocity vector operators, respectively. The Fermi sea term, Eq. (14), is conventionally regarded as intrinsic, devoid of any scattering-driven behavior. In contrast, the Fermi surface term, Eq. (13), encompasses intrinsic, side jump, and skew scattering contributions. Examining Eq. (13), if the bare Green's function G_0 replaces the full Green's function G and the vertex correction is not considered (i.e., $\Gamma^i \to v^i$), it reflects an intrinsic contribution and yields intrinsic AHC $\sigma_{ij}^{\mathrm{int}}$ when combined with the Fermi sea term. When the full Green's function G is used and the vertex correction is not considered (i.e., $\Gamma^i \to v^i$), the side jump contribution to the AHC $\sigma_{ij}^{\mathrm{sj}}$ emerges. Finally, if the full Green's function G is used and the vertex correction is included (i.e., using Γ^i), the skew scattering contribution to the AHC $\sigma_{ij}^{\mathrm{isk}}$ is introduced. The decomposition of AHC can be elucidated through Feynman diagrams, referring to Czaja et al.'s work [56]. By plugging the decomposed AHC into Eqs. (4)–(7), the corresponding components of ANC and ATHC can be obtained accordingly.

In the GD model, the skew scattering term is also known as "intrinsic" skew scattering $\sigma_{ij}^{\mathrm{isk}}$, originally proposed by Sinitsyn and coworkers. [57,58]. Similar to conventional skew scattering, intrinsic skew scattering also arises from the asymmetric part of the collision kernel. However, it converges to a finite value in the clean limit ($\mathcal{V} \to 0$). In contrast, conventional skew scattering is inversely proportional to impurity concentrations and becomes divergent in the clean limit. Diagrammatically speaking, intrinsic skew scattering solely results from Gaussian disorder correlations, while conventional skew scattering involves vertex corrections that include correlators of three or more disorder vertices [56].

The Gaussian disorder model utilized in this study does not explicitly define the types (such as crystal defect or phonon)

and spin structures of impurities. In adopting a "mean-field" approach, the Gaussian disorder model accommodates various scattering channels without delving into the detailed characteristics of the internal nature of scattering sources. Taking into account temperature effects, the microscopic motions within the crystal become more intricate, potentially introducing variations between theoretical calculations and experimental measurements. A comprehensive disorder potential that encompasses all these details could offer a more accurate representation of electronic conductivity and its individual decomposed components. However, the computational treatment of these scattering processes at a detailed microscopic level remains a challenging task for first-principles methods. Thus, the Gaussian disorder model is suitable for Mn_3Sn, identified as a moderately disordered metal, given that its longitudinal conductivity falls within the dirty and intrinsic regimes ($\sigma_{ii} < 10^6$ S/cm) but not the clean regime ($\sigma_{ii} > 10^6$ S/cm), as illustrated in Fig. 3 below.

The first-principles calculations are carried out using the full-potential linearized augmented plane-wave (FP-LAPW) method implemented in the FLEUR code [59]. The exchange-correlation functional is treated within the generalized gradient approximation (GGA) using the Perdew-Burke-Ernzerhof (PBE) parametrization [60]. The spin-orbit coupling is included in all calculations. For Mn_3Sn, a plane-wave cutoff energy of $3.80a_0^{-1}$ is selected, and the experimental lattice constants ($a = b = 5.66$ Å and $c = 4.53$ Å) are adopted. The self-consistent calculations are conducted with a k-point mesh of $16 \times 16 \times 18$. To construct maximally localized Wannier functions, s, p, and d orbitals of Mn atoms and s and p orbitals of Sn atoms are projected onto a uniform k mesh of $8 \times 8 \times 8$ using the WANNIER90 package [61]. To calculate the AHC, an ultradense k mesh of $300 \times 300 \times 300$ is employed. For the calculations of the ANC and ATHC using Eq. (4), the AHC is computed with an energy interval of 0.1 meV.

III. RESULTS AND DISCUSSION

Bulk Mn_3Sn alloy crystallizes in a layered hexagonal structure with the crystallographic space group $P6_3/mmc$. The primitive unit cell consists of two atomic layers stacked along the c axis. Within each layer, the arrangement of three Mn atoms forms a kagome lattice, while the Sn atom is positioned at the center of each hexagon, as depicted in Fig. 1. The spin magnetic moments of the three Mn atoms on the same kagome plane adopt a 120° noncollinear antiferromagnetic order with a Néel temperature T_N of 430 K [20,33]. Our calculated spin magnetic moment for each Mn atom is $3.26\mu_B$, which closely matches the experimental value of $\sim3.0\mu_B$ [20]. Despite being classified as a noncollinear AFM, Mn_3Sn exhibits a very small net magnetic moment ($\sim0.002\mu_B$) [33]. This residual magnetic moment allows for the manipulation of the spin orientation within the kagome plane, for instance, through an external magnetic field. Such spin rotations alter the magnetic group and total energy of the system and consequently impact the anomalous transport properties.

In this context, examining the variations in the AHC tensor due to spin rotation is adequate since the ANC and ATHC have the same symmetry requirements according to Eqs. (4)–(7). The off-diagonal elements of the AHC can be represented

in vector notation as $\boldsymbol{\sigma} = [\sigma^x, \sigma^y, \sigma^z] = [\sigma_{yz}, \sigma_{zx}, \sigma_{xy}]$. Notably, the anomalous Hall vector $\boldsymbol{\sigma}$ can be analogously regarded as a pseudovector, akin to spin. Intuitively, it is more appropriate to consider the magnetic space group over the magnetic point group, as the former encompasses both magnetic and crystal structures through the integration of symmetries, represented as $\mathcal{S}\tau$, where $\mathcal{S}$ denotes a magnetic point group operation and τ signifies a translation operation. For instance, the magnetic point group operations $\mathcal{S} = \mathcal{T}\mathcal{M}_2$ and $\mathcal{T}\mathcal{M}_3$ cannot be capable of maintaining both crystal and magnetic structures when $\theta = 0°$, as illustrated in Fig. 1(a). Only after considering the half-unit-cell translation $\tau_{1/2}$ can the crystal and magnetic structures be preserved. Hence, the comprehensive set of symmetry operations is expressed as $\mathcal{T}\mathcal{M}_2\tau_{1/2}$ and $\mathcal{T}\mathcal{M}_3\tau_{1/2}$, categorizing them under the magnetic space group $Cmc'm'$ for the depicted magnetic structure when $\theta = 0°$. Similarly, for $\theta = 15°$ depicted in Fig. 1(b), the full symmetry operations are $\mathcal{T}\mathcal{M}_3\tau_{1/2}$, falling within the magnetic space group $P2_1'/m'$; for $\theta = 30°$ and 90°, as shown in Figs. 1(c) and 1(d), the complete symmetry operations are $\mathcal{M}_1\tau_{1/2}$ and $\mathcal{T}\mathcal{M}_3\tau_{1/2}$, under the magnetic space group $Cm'cm'$. Nonetheless, we limit our discussion in Fig. 1 to $\mathcal{S}$ operations (excluding τ) and explore how they influence the anomalous Hall vector since τ does not modify the anomalous Hall vector [46], i.e., $\tau\boldsymbol{\sigma} = \boldsymbol{\sigma}$. Therefore, our analysis primarily concentrates on magnetic point groups, an approach we utilized in our earlier studies to investigate various two- and three-dimensional magnetic materials [18,62–68].

Table I underscores that the magnetic point group of Mn_3Sn demonstrates a periodicity of 30°: $m'm'm \rightarrow 2'/m' \rightarrow m'm'm$, as the spin rotates within the kagome plane (x-y plane). Here, it is worth discussing only two nonrepetitive groups, namely $m'm'm$ and $2'/m'$, in relation to four distinct spin configurations ($\theta = 0°$, 15°, 30°, and 90°), as illustrated in Fig. 1. First, for the $m'm'm$ group ($\theta = 0°$), it consists of a mirror symmetry $\mathcal{M}_1$ and two combined symmetries $\mathcal{T}\mathcal{M}_2$ and $\mathcal{T}\mathcal{M}_3$, as depicted in Fig. 1(a). The mirror plane $\mathcal{M}_1$ is perpendicular to the x axis and parallel to the y axis, which leads to a sign change in σ^y and σ^z while leaving σ^x unchanged. Similarly, the mirror plane $\mathcal{M}_2$ (parallel to x axis, perpendicular to y axis) changes the signs of σ^x and σ^z but preserves σ^y. As for the time-reversal symmetry altering the signs of σ^x, σ^y, and σ^z, the combined $\mathcal{T}\mathcal{M}_2$ symmetry changes the sign of σ^y but preserves σ^x and σ^z. Since $\mathcal{M}_3$ (perpendicular to the z axis, parallel to the x-y plane, between two kagome planes) changes the signs of σ^x and σ^y, the combined symmetry $\mathcal{T}\mathcal{M}_3$ preserves σ^x and σ^y. Consequently, for the $m'm'm$ group ($\theta = 0°$), we find $\boldsymbol{\sigma} = [\sigma^x, 0, 0] = [\sigma_{yz}, 0, 0]$. Second, when the spin rotates to 30° within the same $m'm'm$ group, the positions of the $\mathcal{M}_1$ and $\mathcal{M}_2$ mirror planes change accordingly [Fig. 1(c)]. Now, both σ^x and σ^y become nonzero under the $\mathcal{M}_1$ and $\mathcal{T}\mathcal{M}_2$ operations. Hence, for the $m'm'm$ group ($\theta = 30°$), we obtain $\boldsymbol{\sigma} = [\sigma^x, \sigma^y, 0] = [\sigma_{yz}, \sigma_{zx}, 0]$. Third, when $\theta = 90°$, the anomalous Hall vector resorts to the shape $\boldsymbol{\sigma} = [0, \sigma^y, 0] = [0, \sigma_{zx}, 0]$ because the $\mathcal{M}_1$ and $\mathcal{M}_2$ mirror planes are parallel and perpendicular to the x axis, respectively, as shown in Fig. 1(d). Finally, the $2'/m'$ group ($\theta = 15°$) possesses only a combined symmetry operation $\mathcal{T}\mathcal{M}_3$, where the mirror plane $\mathcal{M}_3$ is parallel to the x-y plane and perpendicular to the z

TABLE I. The magnetic space group (MSG), magnetic point group (MPG), and off-diagonal elements of anomalous Hall conductivity for Mn$_3$Sn upon the variation of the spin rotation angle θ within the kagome plane. The presence and absence of off-diagonal elements in the anomalous Hall conductivity are denoted by ✓ and × symbols, respectively.

	θ												
	0°	15°	30°	45°	60°	75°	90°	105°	120°	135°	150°	165°	180°
MSG	$Cmc'm'$	$P2_1'/m'$	$Cm'cm'$	$P2_1'/m'$	$Cmc'm'$	$P2_1'/m'$	$Cm'cm'$	$P2_1'/m'$	$Cmc'm'$	$P2_1'/m'$	$Cm'cm'$	$P2_1'/m'$	$Cmc'm'$
MPG	$m'm'm$	$2'/m'$	$m'm'm$	$2'/m'$	$m'm'm$	$2'/m'$	$m'm'm$	$2'/m'$	$m'm'm$	$2'/m'$	$m'm'm$	$2'/m'$	$m'm'm$
σ_{xy}	×	×	×	×	×	×	×	×	×	×	×	×	×
σ_{yz}	✓	✓	✓	✓	✓	✓	×	✓	✓	✓	✓	✓	✓
σ_{zx}	×	✓	✓	✓	✓	✓	✓	✓	✓	✓	✓	✓	×

axis [Fig. 1(b)]. For this group, the nonzero elements of the AHC are $\boldsymbol{\sigma} = [\sigma^x, \sigma^y, 0] = [\sigma_{yz}, \sigma_{zx}, 0]$. The above results of the symmetry analysis can also be obtained with the Neumann principle [69], wherein all symmetry operations of the corresponding magnetic point group are applied to the conductivity tensor. Additionally, the cluster multipole theory [46] serves as another valuable analysis tool, revealing the shape of the conductivity tensor by assessing the cluster multipole moment, which acts as a macroscopic magnetic order.

In the magnetic group analysis detailed above, we determined all possible nonzero elements of the AHC vector corresponding to different spin rotation angles, as summarized in Table I. Correspondingly, Fig. 2 portrays the total AHC σ_{ij} as a function of θ, computed using two representative disorder parameters. At $\theta = 0°$ or $180°$, only the yz component of AHC exhibits a nonzero value, whereas at $\theta = 90°$, only the zx component is nonzero. For other θ values, both the yz and zx components contribute to the AHC, harmonizing seamlessly with our magnetic group analysis. The AHC is depicted over the range $0 \leqslant \theta \leqslant \pi$, while the results for $\pi \leqslant \theta \leqslant 2\pi$ can be acquired by following the relation $\sigma(\theta) = -\sigma(\theta + \pi)$. This observation arises from the fact that the spin state at $\theta + \pi$ constitutes the time-reversed counterpart of the state at θ, and the AHC maintains an odd symmetry under time-reversal operations [18,66]. Another intriguing observation from Fig. 2 is that the AHC is enhanced across all spin rotation angles when the disorder parameter is decreased. This phenomenon aligns precisely with the disorder-induced amplification of anoma-

lous transport phenomena previously observed in topological semimetals MF$_3$ (M = Mn, Pd) [70].

Based on the dependence of the total AHC σ_{ij} on the longitudinal conductivity σ_{ii}, three distinct scaling relations have been proposed for various magnetic materials [2,49,71,72]: $\sigma_{ij} \propto \sigma_{ii}^2$ or σ_{ii}^1 in the clean regime ($\sigma_{ii} > 10^6$ S/cm), $\sigma_{ij} \propto \sigma_{ii}^0$ in the intrinsic regime ($10^4 < \sigma_{ii} < 10^6$ S/cm), and $\sigma_{ij} \propto \sigma_{ii}^{1.6}$ in the dirty regime ($\sigma_{ii} < 10^4$ S/cm). While earlier theoretical investigations primarily focused on the intrinsic AHE in Mn$_3$Sn [19,45–48], the influence of scattering-dependent extrinsic mechanisms has yet to be explored comprehensively. Figure 3(a) showcases the total AHC σ_{yz} and its decomposition (σ_{yz}^{int}, σ_{yz}^{sj}, and σ_{yz}^{isk}) as a function of longitudinal conductivity σ_{xx} for Mn$_3$Sn in its magnetic ground state ($\theta = 0°$). Notably, Mn$_3$Sn predominantly lies within the dirty and intrinsic regimes because $\sigma_{xx} < 10^6$ S/cm. As σ_{xx} increases, the total AHC σ_{yz} rises and gradually approaches a constant plateau of -230 S/cm for $\sigma_{xx} > 10^4$

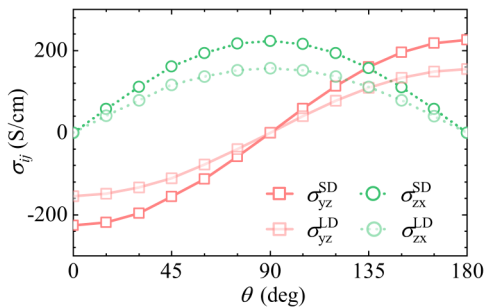FIG. 2. The total AHC (σ_{yz} and σ_{zx}) as a function of θ calculated using a small-disorder (SD) parameter, $\mathcal{V} = 2$ eV$^2 a_0^3$, and a large-disorder (LD) parameter, $\mathcal{V} = 42$ eV$^2 a_0^3$, which correspond to the longitudinal conductivities $\sigma_{xx} = 1.7 \times 10^5$ and 6.4×10^3 S/cm, respectively.

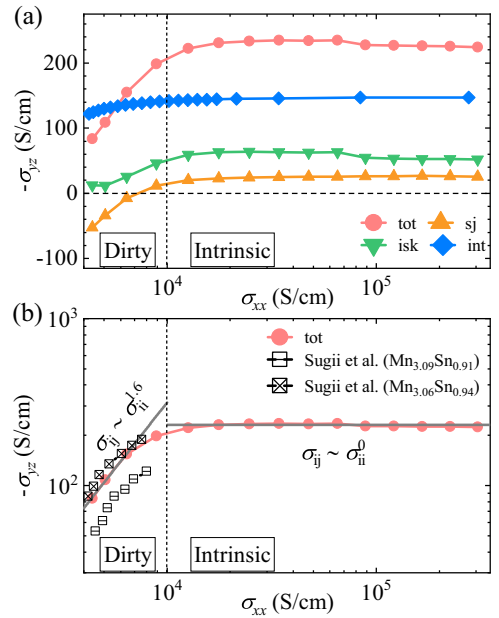

FIG. 3. (a) The total AHC σ_{yz} and its partitioning into the intrinsic (σ_{yz}^{int}), side jump (σ_{yz}^{sj}), and skew scattering (σ_{yz}^{isk}) components as a function of the longitudinal conductivity σ_{xx} for the magnetic ground state ($\theta = 0°$) of Mn$_3$Sn. (b) The scaling relation between σ_{yz} and σ_{xx}. Experimental data from Sugii *et al.* [73] are provided for comparison.

S/cm. In the intrinsic regime, the intrinsic AHC σ_{yz}^{int} ($\approx$ -146 S/cm) plays a dominant role, aligning well with previous theoretical calculations [45–48]. Meanwhile, the extrinsic mechanisms ($\sigma_{yz}^{\text{sj}} + \sigma_{yz}^{\text{isk}}$) take on a secondary role, contributing 34% of the total AHC. Given that the intrinsic mechanism is independent of scattering, it should be much less affected by changes in longitudinal conductivity compared to extrinsic mechanisms.

Our calculations indeed demonstrate that the intrinsic contribution remains fairly stable within the dirty regime ($\sigma_{xx} < 10^4$ S/cm). Conversely, skew scattering rapidly diminishes toward zero, while the side jump experiences a significant increase, primarily governing the declining trend of the total AHC. A recent experimental study reported a reduction in the total AHC as σ_{xx} decreases below 10^4 S/cm [73]. However, that work [73] mentioned that the contribution of the side jump mechanism can be ruled out due to the weak spin-orbit coupling strength of Mn $3d$ electrons, suggesting that the reduction in total AHC is driven by the intrinsic mechanism. In direct comparison, Fig. 3(b) demonstrates the excellent agreement between our calculations and the experimental results [73]. In the dirty regime ($\sigma_{xx} < 10^4$ S/cm), a scaling relation of $\sigma_{yz} \sim \sigma_{xx}^{1.6}$ is evident, highlighting the pronounced significance of the extrinsic side jump mechanism. Consequently, our analysis tends to the conclusion that whereas the intrinsic mechanism dominates in the intrinsic regime, the large reduction of AHC in the dirty regime is primarily attributed to the contribution of the side jump mechanism.

The intrinsic mechanism of AHC stems from the presence of nonvanishing Berry curvature in momentum space and can be largely enhanced by topological features in the band structure like Weyl nodal points. Nevertheless, the link between extrinsic mechanisms of AHC and the underlying band structure remains less clear. Recent theoretical and experimental investigations have illuminated the existence of magnetic Weyl fermions near the Fermi energy E_f in Mn$_3$Sn [33,37,48,74]. As these Weyl points can be interpreted as effective magnetic monopoles in momentum space, the increased Berry curvature in proximity to these points contributes to a substantially amplified AHC. The band structure calculated with spin-orbit coupling for the ground state spin configuration ($\theta = 0°$) of Mn$_3$Sn is presented in Fig. 4(a). The time-reversal symmetry breaking triggers the emergence of multiple pairs of Weyl points at varying energy levels. For our analysis, we focus on those near E_f because they are pertinent to the anomalous transport properties. Owing to the $\mathcal{M}_1$ and $\mathcal{T}\mathcal{M}_2$ symmetries within the $m'm'm$ group, all K points in the first Brillouin zone are equivalent, while two inequivalent M points are labeled M and M'. In the vicinity of the M point, an intersection between a parabolic band and an antiparaboliclike band engenders Weyl points (W_1^+, W_2^-) at $E_f + 36$ meV, accompanied by their counterparts (W_1^-, W_2^+) at $E_f + 72$ meV. However, no Weyl points are present near the M' point. The spatial distribution of Weyl points along the K-M-K path on the $k_z = 0$ plane is showcased in Fig. 4(b). Upon shifting the Fermi energy upward to 36 and 72 meV, the intrinsic AHC around the Weyl points exhibits a sharp increase, as depicted in Fig. 4(c). This observation affirms the inherent enhancement of intrinsic AHC through topological

Weyl nodal structures. Furthermore, Fig. 4(d) illustrates the extrinsic AHC at the same Fermi energies. In contrast to the intrinsic AHC, the extrinsic AHC is primarily distributed along the Fermi surface sheets, indicating a more substantial contribution from the Fermi surfaces compared to the Fermi sea.

Next, we turn to the variation in the anomalous transport properties of Mn$_3$Sn with temperature. To better account for temperature effects, we have opted for a large disorder parameter ($\mathcal{V} = 80$ eV^2 a_0^3) for the calculation of AHC, ANC, and ATHC. Figure 5(a) illustrates the calculated AHC as a function of temperature using Eq. (5), compared with available experimental data. Notably, three previous experimental studies [20,33,73] showed noticeable discrepancies in the magnitude of the AHC. This can be attributed to variations in the chemical composition of the samples, as the Mn:Sn atomic ratio deviates from the ideal 3:1, leading to differences in Mn content across different samples. All of these experimental studies showed a decreasing trend in AHC as the temperature increases, whereas theoretical calculations of AHC exhibit insensitive variation across the entire temperature range. As the temperature increases, phonon thermal dynamics becomes more pronounced, which undoubtedly impacts the anomalous transport properties of magnetic materials. The Gaussian disorder model [56] employed in our work broadly encompasses all mean-field scattering channels. However, the intricate details of electron scattering arising from phonons are not explicitly accounted for. Consequently, as temperature rises, our calculated anomalous transport properties are expected to increase due to their positive temperature-dependent nature.

The total ANC α_{yz} and its components (α_{yz}^{int}, α_{yz}^{sj}, and α_{yz}^{isk}) are computed using Eq. (6) and presented as a function of temperature in Fig. 5(b). It can be observed that the total ANC gradually increases with rising temperature up to 300 K. The extrinsic side jump mechanism contributes significantly to the ANE, even slightly surpassing the contribution of the intrinsic mechanism. On the other hand, the extrinsic skew scattering contribution can be omitted. The upward trend of ANC contrasts with experimental findings, which have demonstrated a decrease in ANC as the temperature goes beyond 150 K [33] or 200 K [34]. Notably, it is worth mentioning that a phase transition from a noncollinear antiferromagnetic structure to a helical spin structure was reported around 200 K [34]. In our calculations, we have exclusively considered a perfect magnetic crystal featuring a 120° noncollinear antiferromagnetic structure, thereby excluding the influence of any additional phase transitions.

Subsequently, we delve into the ATHE of Mn$_3$Sn, akin to the thermal counterpart of AHE, as illustrated in Fig. 5(c). At lower temperatures (below 150 K), the calculated ATHC is in good agreement with experimental results [73]. As the temperature increases, the intrinsic ATHC κ_{yz}^{int} exhibits a monotonic increase, leading to an overall rising trend in the total ATHC κ_{yz}. However, experimental observations have indicated a relatively minor temperature dependence in ATHC [73], fitting the behaviors of our calculated extrinsic ATHC ($\kappa_{yz}^{\text{isk}} + \kappa_{yz}^{\text{sj}}$). The anomalous thermal and electrical transports can be interconnected through the anomalous Lorenz ratio,
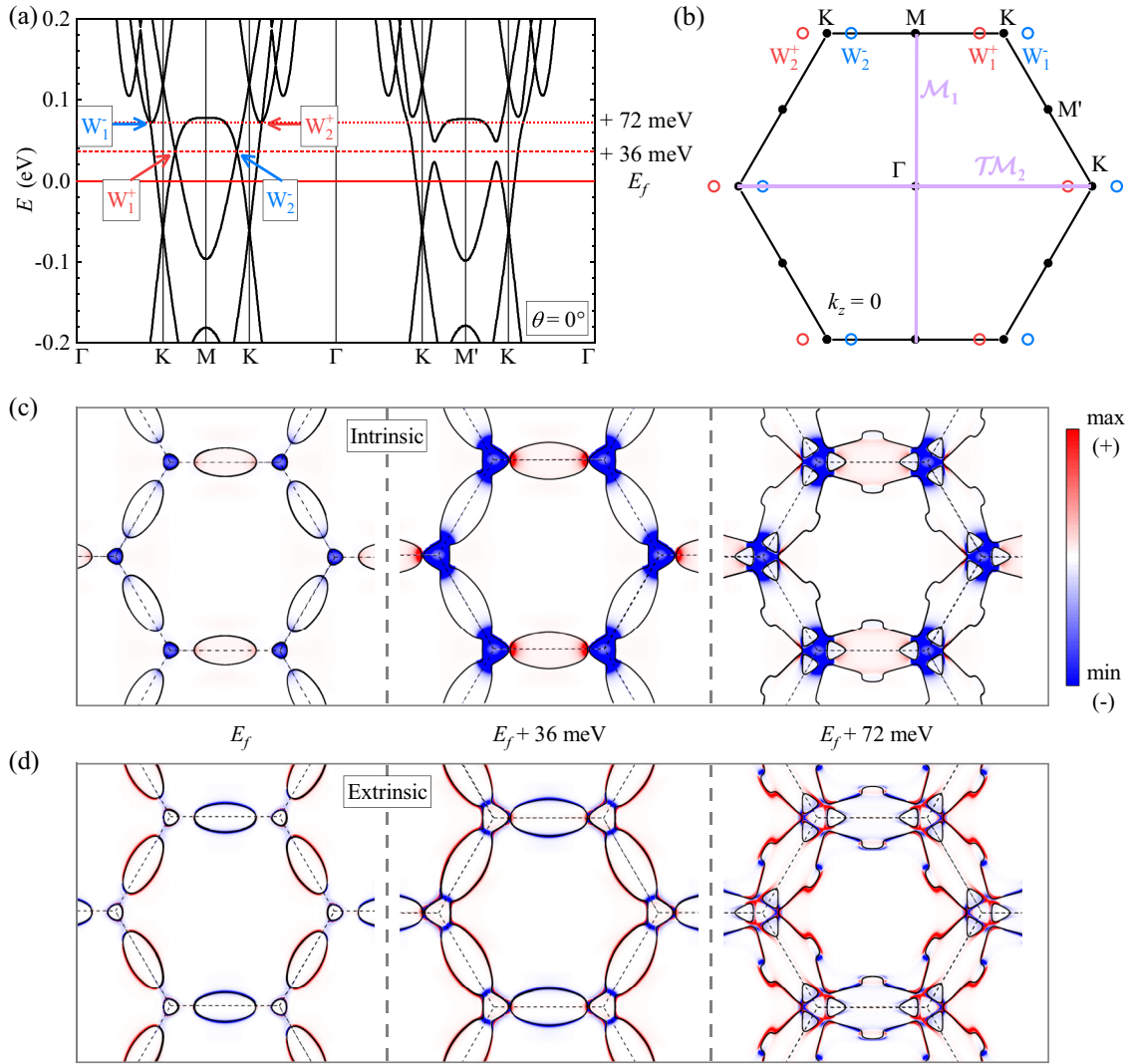
FIG. 4. (a) The band structure of Mn$_3$Sn in its magnetic ground state ($\theta = 0°$). The energy positions of Weyl points ($W_1^{\pm}$ and $W_2^{\pm}$) are indicated by red dashed lines. (b) The distribution of Weyl points on the $k_z = 0$ plane in momentum space. Red and blue circles denote Weyl points with different chiralities. Purple lines represent $\mathcal{M}_1$ and $\mathcal{T}\mathcal{M}_2$ symmetries. (c) and (d) Momentum-resolved intrinsic and extrinsic AHC σ_{yz} (color maps) as well as Fermi surfaces (black lines) on the $k_z = 0$ plane for three distinct Fermi energies (E_f in the left panels, $E_f + 36$ meV in the middle panels, $E_f + 72$ meV in the right panels). The disorder parameter is chosen to be $\mathcal{V} = 2$ eV^2 a_0^3, where the longitudinal conductivity $\sigma_{xx} = 1.7 \times 10^5$ S/cm.

defined as

$$L_{ij} = \kappa_{ij}/(\sigma_{ij}T), \tag{17}$$

which has been employed to judge the intrinsic and scattering contributions to the AHE [15–17]. Plugging the intrinsic, side jump, and skew scattering parts of the AHC and ATHC into Eq. (17), L_{ij} can be separately analyzed as $L_{ij}^{\text{int/sj/isk}} = \kappa_{ij}^{\text{int/sj/isk}}/(\sigma_{ij}^{\text{int/sj/isk}}T)$, where L_{ij}^{int} represents the intrinsic contribution and L_{ij}^{sj} and L_{ij}^{isk} are the extrinsic contributions from side jump and skew scattering, respectively. As the temperature approaches zero, L_{ij} converges to the free-electron Lorenz number, commonly referred to as the Wiedemann-Franz law:

$$L_{ij}(T \rightarrow 0) \approx L_0 = \frac{\pi^2 k_B^2}{3e^2} = 2.44 \times 10^{-8} \text{ V}^2/\text{K}^2. \tag{18}$$

Examining Fig. 5(d), we observe that across the entire temperature range, the calculated L_{yz}^{int} closely aligns with L_0. This indicates that the transverse charge and heat currents induced by intrinsic mechanism flow in a nearly dissipationless way. However, L_{yz}^{sj}, L_{yz}^{isk}, and L_{yz}^{tot} are close to L_0 only when the temperature is less than 50 K. As the temperature rises, the transverse heat current carried by conducting electrons is expected to experience progressively increased dissipation due to inelastic scattering with phonons. For instance, above 50 K, experimentally measured L_{yz} for Mn$_{3.06}$Sn$_{0.94}$ [73] deviates noticeably from L_0, signaling a crossover in the dominant role from an intrinsic mechanism to extrinsic mechanisms. This is consistent with our calculations of extrinsic contributions to the anomalous Lorenz ratio as the temperature increases. However, for the Mn$_{3.09}$Sn$_{0.91}$ sample [73] and another experimental study of Mn$_3$Sn [34], the
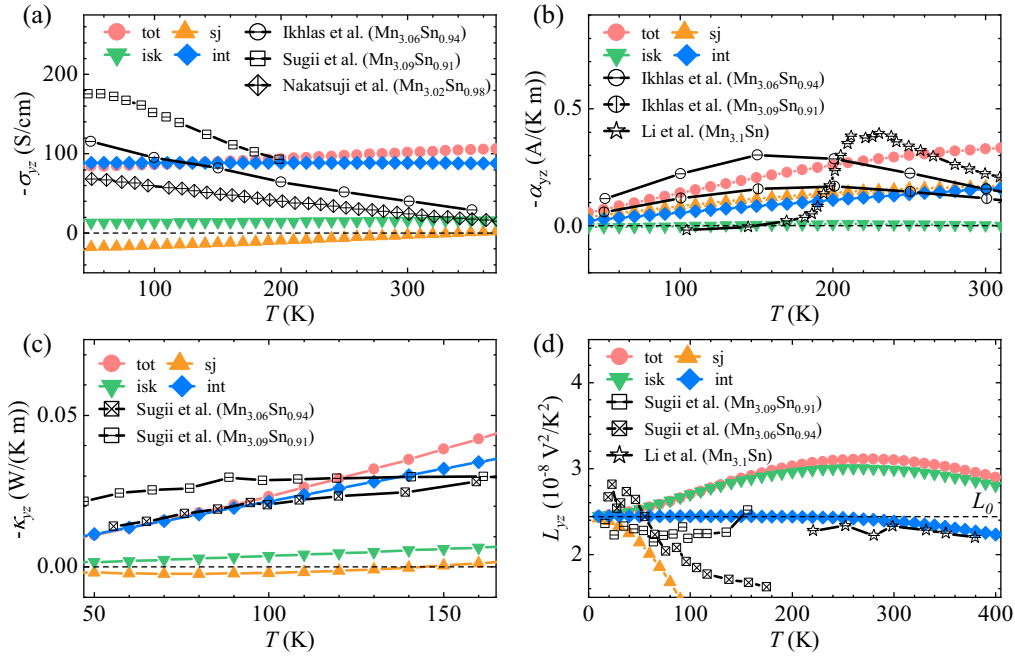
FIG. 5. (a) The temperature-dependent AHC in comparison to experimental data from Nakatsuji *et al.* [20], and Ikhlas *et al.* [33], and Sugii *et al.* [73]. (b) The temperature-dependent ANC in comparison to experimental data from Ikhlas *et al.* [33] and Li *et al.* [34]. (c) The temperature-dependent ATHC in comparison to experimental data from Sugii *et al.* [73]. (d) The anomalous Lorenz ratio in comparison to experimental data from Li *et al.* [34] and Sugii *et al.* [73]. The horizontal dashed line in (d) marks the free-electron Lorenz number $L_0 = 2.44 \times 10^{-8}$ V^2/K^2. The disorder parameter is selected to be $\mathcal{V} = 80$ eV$^2 a_0^3$, where the longitudinal conductivity $\sigma_{xx} = 0.44 \times 10^4$ S/cm, falling into the dirty regime.

deviation of L_{yz} from L_0 is not substantial, indicating the potential persistence of the intrinsic mechanism's predominance over the extrinsic ones. Thus, in this work, we not only demonstrate that the dissipationless intrinsic transverse charge and heat currents adhere to the Wiedemann-Franz law across the entire temperature range (0–300 K) in the noncollinear AFM Mn$_3$Sn but also show that extrinsic transverse charge and heat currents induced by scattering or disorder will gradually deviate from the Wiedemann-Franz law as the temperature increases.

IV. SUMMARY

In summary, we have systematically studied the intrinsic and extrinsic anomalous Hall, anomalous Nernst, and anomalous thermal Hall effects in noncollinear antiferromagnetic Mn$_3$Sn, utilizing advanced first-principle calculations and magnetic group analysis. In our study, the intrinsic contribution is associated with the Berry phase effect of relativistic bands within a pristine crystal, free from impurities. All additional contributions arising from scatterings on impurities or disorder are classified as extrinsic. The spin-independent impurity potential utilized in our study can be understood as representing nonmagnetic impurities in magnetic materials. With the incorporation of spin-orbit coupling, the electron's spin becomes intricately dependent on the modification of its orbital angular momentum during scattering. Consequently, the transverse flow of spin-polarized electrons induced by scattering on nonmagnetic

impurities is indeed feasible. The definitions of intrinsic and extrinsic contributions to the anomalous transport properties align with established conventions in the majority of previous research.

We first identified the nonvanishing tensor elements of anomalous Hall conductivity for diverse coplanar noncollinear spin configurations, according to symmetry requirements under relevant magnetic point groups. Upon the collective rotation of all spins within the kagome plane, the anomalous Hall conductivity showcases periodic patterns, giving rise to a pronounced magnetic anisotropy. Previous theoretical works primarily focused on studying the intrinsic anomalous transport properties of Mn$_3$Sn through Berry curvature calculations, with relatively less attention given to extrinsic mechanisms. Through computations of the total anomalous Hall conductivity and its constituent components, we have unveiled that the intrinsic mechanism uniformly dominates within the intrinsic regime, especially when the longitudinal conductivity σ_{xx} surpasses 10^4 S/cm. The intrinsic mechanism can be traced to substantial Berry curvatures encircling Weyl points proximate to the Fermi energy. In the realm of the dirty regime ($\sigma_{xx} < 10^4$ S/cm), extrinsic mechanisms, notably the side jump, emerge as potent contributors, which brings our theoretical results closer to experimental measurements. This extrinsic anomalous Hall conductivity predominantly stems from electronic states positioned precisely at the Fermi surfaces. Moreover, our findings with regard to the anomalous thermal Hall effect and anomalous Lorenz ratio compare well with experimental outcomes at

low temperatures, consistently indicating the dominant role of the intrinsic mechanism. As the temperature rises, a certain degree of deviation between theoretical and experimental results becomes apparent. These deviations may be attributed to enhanced phonon scattering and increased complexity in the internal structure of the crystal, factors that are not fully accounted for in the Gaussian disorder model. Through these comprehensive insights, our study has substantially enriched the understanding of anomalous transport phenomena in noncollinear antiferromagnetic Mn_3Sn. Furthermore, our work offers valuable perspectives for potential applications in the realms of spintronics and spin caloritronics, harnessing the distinctive attributes of noncollinear antiferromagnetic materials.

[1] E. Hall, XVIII. On the "rotational coefficient" in nickel and cobalt, London, Edinburgh, Dublin Philos. Mag. J. Sci. **12**, 157 (1881).

[2] N. Nagaosa, J. Sinova, S. Onoda, A. H. MacDonald, and N. P. Ong, Anomalous Hall effect, Rev. Mod. Phys. **82**, 1539 (2010).

[3] R. Karplus and J. M. Luttinger, Hall effect in ferromagnetics, Phys. Rev. **95**, 1154 (1954).

[4] G. Sundaram and Q. Niu, Wave-packet dynamics in slowly perturbed crystals: Gradient corrections and Berry-phase effects, Phys. Rev. B **59**, 14915 (1999).

[5] Y. Yao, L. Kleinman, A. H. MacDonald, J. Sinova, T. Jungwirth, D.-s. Wang, E. Wang, and Q. Niu, First principles calculation of anomalous Hall conductivity in ferromagnetic bcc Fe, Phys. Rev. Lett. **92**, 037204 (2004).

[6] J. Smit, The spontaneous Hall effect in ferromagnetics I, Physica (Amsterdam) **21**, 877 (1955).

[7] J. Smit, The spontaneous Hall effect in ferromagnetics II, Physica (Amsterdam) **24**, 39 (1958).

[8] L. Berger, Side-jump mechanism for the Hall effect of ferromagnets, Phys. Rev. B **2**, 4559 (1970).

[9] D. Xiao, Y. Yao, Z. Fang, and Q. Niu, Berry-phase effect in anomalous thermoelectric transport, Phys. Rev. Lett. **97**, 026603 (2006).

[10] T. Qin, Q. Niu, and J. Shi, Energy magnetization and the thermal Hall effect, Phys. Rev. Lett. **107**, 236601 (2011).

[11] T. Jungwirth, Q. Niu, and A. H. MacDonald, Anomalous Hall effect in ferromagnetic semiconductors, Phys. Rev. Lett. **88**, 207208 (2002).

[12] Z. Fang, N. Nagaosa, K. S. Takahashi, A. Asamitsu, R. Mathieu, T. Ogasawara, H. Yamada, M. Kawasaki, Y. Tokura, and K. Terakura, The anomalous Hall effect and magnetic monopoles in momentum space, Science **302**, 92 (2003).

[13] S. Onoda, N. Sugimoto, and N. Nagaosa, Intrinsic versus extrinsic anomalous Hall effect in ferromagnets, Phys. Rev. Lett. **97**, 126602 (2006).

[14] S. Onoda, N. Sugimoto, and N. Nagaosa, Quantum transport theory of anomalous electric, thermoelectric, and thermal Hall effects in ferromagnets, Phys. Rev. B **77**, 165103 (2008).

[15] Y. Onose, Y. Shiomi, and Y. Tokura, Lorenz number determination of the dissipationless nature of the anomalous Hall effect in itinerant ferromagnets, Phys. Rev. Lett. **100**, 016601 (2008).

[16] Y. Shiomi, Y. Onose, and Y. Tokura, Extrinsic anomalous Hall effect in charge and heat transport in pure iron, $Fe_{0.997}Si_{0.003}$, and $Fe_{0.97}Co_{0.03}$, Phys. Rev. B **79**, 100404(R) (2009).

[17] Y. Shiomi, Y. Onose, and Y. Tokura, Effect of scattering on intrinsic anomalous Hall effect investigated by Lorenz ratio, Phys. Rev. B **81**, 054414 (2010).

[18] X. Zhou, J.-P. Hanke, W. Feng, F. Li, G.-Y. Guo, Y. Yao, S. Blügel, and Y. Mokrousov, Spin-order dependent anomalous Hall effect and magneto-optical effect in the noncollinear antiferromagnets Mn_3XN with $X =$ Ga, Zn, Ag, or Ni, Phys. Rev. B **99**, 104428 (2019).

[19] H. Chen, Q. Niu, and A. H. MacDonald, Anomalous Hall effect arising from noncollinear antiferromagnetism, Phys. Rev. Lett. **112**, 017205 (2014).

[20] S. Nakatsuji, N. Kiyohara, and T. Higo, Large anomalous Hall effect in a non-collinear antiferromagnet at room temperature, Nature (London) **527**, 212 (2015).

[21] N. Kiyohara, T. Tomita, and S. Nakatsuji, Giant anomalous Hall effect in the chiral antiferromagnet Mn_3Ge, Phys. Rev. Appl. **5**, 064009 (2016).

[22] A. K. Nayak, J. E. Fischer, Y. Sun, B. Yan, J. Karel, A. C. Komarek, C. Shekhar, N. Kumar, W. Schnelle, J. Kübler, C. Felser, and S. S. P. Parkin, Large anomalous Hall effect driven by a nonvanishing Berry curvature in the noncolinear antiferromagnet Mn_3Ge, Sci. Adv. **2**, e1501870 (2016).

[23] X. Marti, I. Fina, C. Frontera, J. Liu, P. Wadley, Q. He, R. J. Paull, J. D. Clarkson, J. Kudrnovský, I. Turek, J. Kuneš, D. Yi, J.-H. Chu, C. T. Nelson, L. You, E. Arenholz, S. Salahuddin, J. Fontcuberta, T. Jungwirth, and R. Ramesh, Room-temperature antiferromagnetic memory resistor, Nat. Mater. **13**, 367 (2014).

[24] P. Wadley *et al.*, Electrical switching of an antiferromagnet, Science **351**, 587 (2016).

[25] A. Kirilyuk, A. V. Kimel, and T. Rasing, Ultrafast optical manipulation of magnetic order, Rev. Mod. Phys. **82**, 2731 (2010).

[26] C. Tzschaschel, K. Otani, R. Iida, T. Shimura, H. Ueda, S. Günther, M. Fiebig, and T. Satoh, Ultrafast optical excitation of coherent magnons in antiferromagnetic NiO, Phys. Rev. B **95**, 174407 (2017).

[27] T. Kampfrath, A. Sell, G. Klatt, A. Pashkin, S. Mährlein, T. Dekorsy, M. Wolf, M. Fiebig, A. Leitenstorfer, and R. Huber, Coherent terahertz control of antiferromagnetic spin waves, Nat. Photonics **5**, 31 (2011).

[28] A. Pashkin, A. Sell, T. Kampfrath, and R. Huber, Electric and magnetic terahertz nonlinearities resolved on the sub-cycle scale, New J. Phys. **15**, 065003 (2013).

[29] T. Jungwirth, X. Marti, P. Wadley, and J. Wunderlich, Antiferromagnetic spintronics, Nat. Nanotechnol. **11**, 231 (2016).

[30] V. Baltz, A. Manchon, M. Tsoi, T. Moriyama, T. Ono, and Y. Tserkovnyak, Antiferromagnetic spintronics, Rev. Mod. Phys. **90**, 015005 (2018).

[31] T. Matsuda, N. Kanda, T. Higo, N. P. Armitage, S. Nakatsuji, and R. Matsunaga, Room-temperature terahertz anomalous Hall effect in Weyl antiferromagnet Mn_3Sn thin films, Nat. Commun. **11**, 909 (2020).

[32] L. Xu, X. Li, X. Lu, C. Collignon, H. Fu, J. Koo, B. Fauqué, B. Yan, Z. Zhu, and K. Behnia, Finite-temperature violation of the anomalous transverse Wiedemann-Franz law, Sci. Adv. **6**, eaaz3522 (2020).

[33] M. Ikhlas, T. Tomita, T. Koretsune, M.-T. Suzuki, D. Nishio-Hamane, R. Arita, Y. Otani, and S. Nakatsuji, Large anomalous Nernst effect at room temperature in a chiral antiferromagnet, Nat. Phys. **13**, 1085 (2017).

[34] X. Li, L. Xu, L. Ding, J. Wang, M. Shen, X. Lu, Z. Zhu, and K. Behnia, Anomalous Nernst and Righi-Leduc effects in Mn_3Sn: Berry curvature and entropy flow, Phys. Rev. Lett. **119**, 056601 (2017).

[35] T. Higo, H. Man, D. B. Gopman, L. Wu, T. Koretsune, O. M. J. van 't Erve, Y. P. Kabanov, D. Rees, Y. Li, M.-T. Suzuki, S. Patankar, M. Ikhlas, C. L. Chien, R. Arita, R. D. Shull, J. Orenstein, and S. Nakatsuji, Large magneto-optical Kerr effect and imaging of magnetic octupole domains in an antiferromagnetic metal, Nat. Photonics **12**, 73 (2018).

[36] H. C. Zhao, H. Xia, S. Hu, Y. Y. Lv, Z. R. Zhao, J. He, E. Liang, G. Ni, L. Y. Chen, X. P. Qiu, S. M. Zhou, and H. B. Zhao, Large ultrafast-modulated Voigt effect in noncollinear antiferromagnet Mn_3Sn, Nat. Commun. **12**, 5266 (2021).

[37] K. Kuroda *et al.*, Evidence for magnetic Weyl fermions in a correlated metal, Nat. Mater. **16**, 1090 (2017).

[38] T. Chen, T. Tomita, S. Minami, M. Fu, T. Koretsune, M. Kitatani, I. Muhammad, D. Nishio-Hamane, R. Ishii, F. Ishii, R. Arita, and S. Nakatsuji, Anomalous transport due to Weyl fermions in the chiral antiferromagnets Mn_3X, X=Sn, Ge, Nat. Commun. **12**, 572 (2021).

[39] M. Kimata, H. Chen, K. Kondou, S. Sugimoto, P. K. Muduli, M. Ikhlas, Y. Omori, T. Tomita, A. H. MacDonald, S. Nakatsuji, and Y. Otani, Magnetic and magnetic inverse spin Hall effects in a non-collinear antiferromagnet, Nature (London) **565**, 627 (2019).

[40] Y. Takeuchi, Y. Yamane, J.-Y. Yoon, R. Itoh, B. Jinnai, S. Kanai, J. Ieda, S. Fukami, and H. Ohno, Chiral-spin rotation of noncollinear antiferromagnet by spin–orbit torque, Nat. Mater. **20**, 1364 (2021).

[41] T. Higo, K. Kondou, T. Nomoto, M. Shiga, S. Sakamoto, X. Chen, D. Nishio-Hamane, R. Arita, Y. Otani, S. Miwa, and S. Nakatsuji, Perpendicular full switching of chiral antiferromagnetic order by current, Nature (London) **607**, 474 (2022).

[42] L. Ye, M. Kang, J. Liu, F. von Cube, C. R. Wicker, T. Suzuki, C. Jozwiak, A. Bostwick, E. Rotenberg, D. C. Bell, L. Fu, R. Comin, and J. G. Checkelsky, Massive Dirac fermions in a ferromagnetic kagome metal, Nature (London) **555**, 638 (2018).

[43] D. F. Liu, A. J. Liang, E. K. Liu, Q. N. Xu, Y. W. Li, C. Chen, D. Pei, W. J. Shi, S. K. Mo, P. Dudin, T. Kim, C. Cacho, G. Li, Y. Sun, L. X. Yang, Z. K. Liu, S. S. P. Parkin, C. Felser, and Y. L. Chen, Magnetic Weyl semimetal phase in a kagomé crystal, Science **365**, 1282 (2019).

[44] J.-X. Yin *et al.*, Quantum-limit Chern topological magnetism in $TbMn_6Sn_6$, Nature (London) **583**, 533 (2020).

[45] J. Kübler and C. Felser, Non-collinear antiferromagnets and the anomalous Hall effect, Europhys. Lett. **108**, 67001 (2014).

[46] M.-T. Suzuki, T. Koretsune, M. Ochi, and R. Arita, Cluster multipole theory for anomalous Hall effect in antiferromagnets, Phys. Rev. B **95**, 094406 (2017).

[47] G.-Y. Guo and T.-C. Wang, Large anomalous Nernst and spin Nernst effects in the noncollinear antiferromagnets Mn_3X ($X =$ Sn, Ge, Ga), Phys. Rev. B **96**, 224415 (2017).

[48] Y. Zhang, Y. Sun, H. Yang, J. Železný, S. P. P. Parkin, C. Felser, and B. Yan, Strong anisotropic anomalous Hall effect and spin Hall effect in the chiral antiferromagnetic compounds Mn_3X ($X =$ Ge, Sn, Ga, Ir, Rh, and Pt), Phys. Rev. B **95**, 075128 (2017).

[49] S.-Y. Yang, Y. Wang, B. R. Ortiz, D. Liu, J. Gayles, E. Derunova, R. Gonzalez-Hernandez, L. Šmejkal, Y. Chen, S. S. P. Parkin, S. D. Wilson, E. S. Toberer, T. McQueen, and M. N. Ali, Giant, unconventional anomalous Hall effect in the metallic frustrated magnet candidate, KV_3Sb_5, Sci. Adv. **6**, eabb6003 (2020).

[50] F. H. Yu, T. Wu, Z. Y. Wang, B. Lei, W. Z. Zhuo, J. J. Ying, and X. H. Chen, Concurrence of anomalous Hall effect and charge density wave in a superconducting topological kagome metal, Phys. Rev. B **104**, L041103 (2021).

[51] D. Singh, J. Nag, S. Yadam, V. Ganesan, A. Alam, and K. G. Suresh, Colossal anomalous Hall conductivity and topological Hall effect in ferromagnetic kagome metal Nd_3Al, arXiv:2111.12944.

[52] N. W. Ashcroft and N. D. Mermin, *Solid State Physics* (Saunders College Publishing, Philadelphia, 1976).

[53] H. van Houten, L. W. Molenkamp, C. W. J. Beenakker, and C. T. Foxon, Thermo-electric properties of quantum point contacts, Semicond. Sci. Technol. **7**, B215 (1992).

[54] K. Behnia, *Fundamentals of Thermoelectricity* (Oxford University Press, Oxford, 2015).

[55] R. Kubo, Statistical-mechanical theory of irreversible processes. I. General theory and simple applications to magnetic and conduction problems, J. Phys. Soc. Jpn. **12**, 570 (1957).

[56] P. Czaja, F. Freimuth, J. Weischenberg, S. Blügel, and Y. Mokrousov, Anomalous Hall effect in ferromagnets with Gaussian disorder, Phys. Rev. B **89**, 014411 (2014).

[57] N. A. Sinitsyn, A. H. MacDonald, T. Jungwirth, V. K. Dugaev, and J. Sinova, Anomalous Hall effect in a two-dimensional Dirac band: The link between the Kubo-Streda formula and the semiclassical Boltzmann equation approach, Phys. Rev. B **75**, 045315 (2007).

[58] N. A. Sinitsyn, Semiclassical theories of the anomalous Hall effect, J. Phys.: Condens. Matter **20**, 023201 (2008).

[59] D. Wortmann *et al.*, FLEUR, 2023, Zenodo, www.flapw.de.

[60] J. P. Perdew, K. Burke, and M. Ernzerhof, Generalized gradient approximation made simple, Phys. Rev. Lett. **77**, 3865 (1996).

[61] G. Pizzi *et al.*, Wannier90 as a community code: New features and applications, J. Phys.: Condens. Matter **32**, 165902 (2020).

[62] X. Zhou, R.-W. Zhang, Z. Zhang, D.-S. Ma, W. Feng, Y. Mokrousov, and Y. Yao, Fully spin-polarized nodal loop semimetals in alkaline-metal monochalcogenide monolayers, J. Phys. Chem. Lett. **10**, 3101 (2019).

[63] X. Zhou, J.-P. Hanke, W. Feng, S. Blügel, Y. Mokrousov, and Y. Yao, Giant anomalous Nernst effect in noncollinear antiferromagnetic Mn-based antiperovskite nitrides, Phys. Rev. Mater. **4**, 024408 (2020).

[64] R.-W. Zhang, X. Zhou, Z. Zhang, D.-S. Ma, Z.-M. Yu, W. Feng, and Y. Yao, Weyl monoloop semi-half-metal and tunable anomalous Hall effect, Nano Lett. **21**, 8749 (2021).

[65] X. Zhou, W. Feng, Y. Li, and Y. Yao, Spin-chirality-driven quantum anomalous and quantum topological Hall effects in chiral magnets, Nano Lett. **23**, 5680 (2023).

[66] X. Yang, X. Zhou, W. Feng, and Y. Yao, Tunable magneto-optical effect, anomalous Hall effect, and anomalous Nernst effect in the two-dimensional room-temperature ferromagnet $1T$-$CrTe_2$, Phys. Rev. B **103**, 024436 (2021).

[67] X. Yang, X. Zhou, W. Feng, and Y. Yao, Strong magneto-optical effect and anomalous transport in the two-dimensional van der Waals magnets Fe_nGeTe ($n = 3, 4, 5$), Phys. Rev. B **104**, 104427 (2021).

[68] X. Yang, P. Yang, X. Zhou, W. Feng, and Y. Yao, First- and second-order magneto-optical effects and intrinsically anomalous transport in the two-dimensional van der Waals layered magnets $CrXY$ (X = S, Se, Te; Y = Cl, Br, I), Phys. Rev. B **106**, 054408 (2022).

[69] M. Seemann, D. Ködderitzsch, S. Wimmer, and H. Ebert, Symmetry-imposed shape of linear response tensors, Phys. Rev. B **92**, 155138 (2015).

[70] X. Zhou, R.-W. Zhang, X. Yang, X.-P. Li, W. Feng, Y. Mokrousov, and Y. Yao, Disorder- and topology-enhanced fully spin-polarized currents in nodal chain spin-gapless semimetals, Phys. Rev. Lett. **129**, 097201 (2022).

[71] M. Huang, S. Wang, Z. Wang, P. Liu, J. Xiang, C. Feng, X. Wang, Z. Zhang, Z. Wen, H. Xu, G. Yu, Y. Lu, W. Zhao, S. A. Yang, D. Hou, and B. Xiang, Colossal anomalous Hall effect in ferromagnetic van der Waals $CrTe_2$, ACS Nano **15**, 9759 (2021).

[72] T. Miyasato, N. Abe, T. Fujii, A. Asamitsu, S. Onoda, Y. Onose, N. Nagaosa, and Y. Tokura, Crossover behavior of the anomalous Hall effect and anomalous Nernst effect in itinerant ferromagnets, Phys. Rev. Lett. **99**, 086602 (2007).

[73] K. Sugii, Y. Imai, M. Shimozawa, M. Ikhlas, N. Kiyohara, T. Tomita, M.-T. Suzuki, T. Koretsune, R. Arita, S. Nakatsuji, and M. Yamashita, Anomalous thermal Hall effect in the topological antiferromagnetic state, arXiv:1902.06601.

[74] H. Yang, Y. Sun, Y. Zhang, W.-J. Shi, S. S. P. Parkin, and B. Yan, Topological Weyl semimetals in the chiral antiferromagnetic materials Mn_3Ge and Mn_3Sn, New J. Phys. **19**, 015008 (2017).